

A first principles investigation of cubic BaRuO₃: A Hund's metal

Nagamalleswararao Dasari^{1,*}, S. R. K. C. Sharma Yamijala², Manish Jain³, T. Saha Dasgupta⁴, Juana Moreno^{5,6}, Mark Jarrell^{5,6}, and N. S. Vidhyadhiraja^{1†}

¹*Theoretical Sciences Unit, Jawaharlal Nehru Centre For Advanced Scientific Research, Jakkur, Bangalore 560064, India.*

²*Chemistry and Physics of Materials Unit, Jawaharlal Nehru Centre For Advanced Scientific Research, Jakkur, Bangalore 560064, India.*

³*Department of Physics, Indian Institute of Science, Bangalore 560012, India*

⁴*S. N. Bose Centre for Basic Sciences, Kolkata 700 098, India.*

⁵*Department of Physics & Astronomy, Louisiana State University, Baton Rouge, LA 70803-4001, USA. and*

⁶*Center for Computation and Technology, Louisiana State University, Baton Rouge, LA 70803, USA.*

A first-principles investigation of cubic-BaRuO₃, by combining density functional theory with dynamical mean-field theory and a hybridization expansion continuous time quantum Monte-Carlo solver, has been carried out. Non-magnetic calculations with appropriately chosen on-site Coulomb repulsion, U and Hund's exchange, J , for single-particle dynamics and static susceptibility show that cubic-BaRuO₃ is in a spin-frozen state at temperatures above the ferromagnetic transition point. A strong red shift with increasing J of the peak in the real frequency dynamical susceptibility indicates a dramatic suppression of the Fermi liquid coherence scale as compared to the bare parameters in cubic-BaRuO₃. The self-energy also shows clear deviation from Fermi liquid behaviour that manifests in the single-particle spectrum. Such a clean separation of energy scales in this system provides scope for an incoherent spin-frozen (SF) phase, that extends over a wide temperature range, to manifest in non-Fermi liquid behaviour and to be the precursor for the magnetically ordered ground state.

I. Introduction

Transition metal oxides (TMOs) have occupied a unique and very significant position in the investigations of correlated electron systems. The interplay of spin, charge and orbital degrees of freedom in the partially filled and localized 3d and 4d orbitals leads to a rich set of phenomena including high temperature superconductivity, colossal magneto-resistance and the Mott metal-insulator transition. Due to the extended nature of 4d orbitals, the corresponding TMOs exhibit strong hybridization with oxygen. This leads to a large crystal field splitting that could be of the order of the local screened Coulomb interaction (U) and a broad 4d band of width W . As a consequence, these materials prefer a low spin state rather than the high spin state.

Furthermore, the wide d-band in 4d-orbital based TMOs such as Ruthenates leads to a moderate screened Coulomb interaction $U \simeq W$ as compared to the much narrower d-band in 3d-orbital based TMOs¹. Surprisingly however, most of the Ru-based TMOs show strong correlation effects that are reflected in the enhanced linear coefficient of specific heat γ . A few of such ruthenates are mentioned in table-I, where we have also indicated the magnetic order of the ground state as well as the effective mass computed as the ratio of experimentally^{1,2} measured γ to γ_{LDA} , computed² within a local density approximation (LDA). The origin of such enhanced effective mass could be a local Coulomb repulsion induced proximity to a insulating state. An alternative origin could be Hund's^{1,3-5} coupling J (intra-atomic exchange), which, as has been shown recently for several materials, especially Ruthenates^{3,6,7}, leads to their characterization as 'Hund's metals'. A prominent member of this class is

BaRuO₃ which, depending on synthesis conditions, can

TABLE I. Magnetic ground state and the ratio of γ to γ_{LDA} for 4d Ru-based compounds

| Compound | Magnetic order | $\frac{\gamma}{\gamma_{LDA}}$ |
|--|----------------|-------------------------------|
| Sr ₂ RuO ₄ | PM | 4 |
| Sr ₃ Ru ₂ O ₇ | PM | 10 |
| CaRuO ₃ | PM | 7 |
| SrRuO ₃ | FM < 160 K | 4 |
| 3C-BaRuO ₃ | FM < 60 K | — |
| 4H-BaRuO ₃ | PM | 3.37 |
| 6H-BaRuO ₃ | PM | 3.37 |
| 9R-BaRuO ₃ | PI | 1.54 |

exist in four polytypes⁸. These are nine-layered rhombohedral (9R), four-layered hexagonal (4H), six-layered hexagonal (6H) and cubic (3C). The 9R has a paramagnetic insulating (PI) ground state while 4H and 6H are paramagnetic metals (PM).

The 3C-BaRuO₃ polytype is a ferromagnetic metal with Curie temperature, $T_c = 60$ K, which is much smaller than the value of $T_c (= 160$ K) in SrRuO₃⁹. The experimental value of the saturated magnetic moment of 3C-BaRuO₃⁸ is $0.8 \mu_B/\text{Ru}$, which is far less than $2.8 \mu_B/\text{Ru}$, expected for a low spin state of 4d Ru. It is also smaller than measured value of $1.4 \mu_B/\text{Ru}$ in SrRuO₃⁹. The observed effective magnetic moment (μ_{eff}) in the

paramagnetic phase of BaRuO₃ and SrRuO₃, is however, very close to the S=1 moment. From table I, we can readily understand that electron correlations in 4H-BaRuO₃ and 6H-BaRuO₃ are comparable with SrRuO₃ and in case of 9R-BaRuO₃ they are weak. Although the strength of electron correlations in 3C-BaRuO₃ is still unknown, a non-Fermi liquid behavior in the experimental measured resistivity^{8,10}, i.e., $\rho(T) \propto T^{1.85}$ in the ferromagnetic phase and its cross-over to $T^{0.5}$ in the paramagnetic phase (similar to SrRuO₃¹¹ and CaRuO₃¹² compounds), hints towards a strongly correlated system¹.

In the present work, the following questions have been addressed: Is 3C-BaRuO₃ a correlated metal or not? If yes, then what is the origin and strength of correlations? What is the probable origin of non-Fermi liquid (NFL) signature in the resistivity^{8,10}? We have employed the dynamical mean field theory (DMFT) framework in combination with an *ab initio* method¹³, namely density functional theory (DFT) within the generalized gradient approximation (GGA)¹⁴. In the DMFT¹⁵ framework, a lattice problem may be mapped on to a single impurity Anderson model with a self-consistently determined bath. The resulting quantum impurity problem has been solved by using hybridization expansion^{16,17} continuous-time quantum Monte-Carlo algorithm (HY-CTQMC). The main finding is that 3C-BaRuO₃ is a Hund's correlated metal. Furthermore we find that 3C-BaRuO₃ is in a spin-frozen state at temperatures in the neighbourhood of the experimental ferromagnetic transition temperature. This state, we speculate, is the precursor of the ferromagnetic ground state and also a possible origin of the experimentally observed NFL behavior in resistivity.

The rest of the paper is organised as follows. In section II, we describe the DFT details and Wannier projection briefly. In Section III, we describe our results from GGA+DMFT(CTQMC) for 3C-BaRuO₃. We present our conclusions in the final section.

II. Details of the density functional theory calculations and results

The 3C polytype of BaRuO₃ belongs to the space group of *Pm-3m* which corresponds to an ideal cubic perovskite structure, while the closely related CaRuO₃ and SrRuO₃ crystallize in an orthorhombic distorted perovskite structure of space group *Pnma*⁸. A significant structural change from CaRuO₃ to SrRuO₃ and to BaRuO₃ is a decrease in bending angle⁸ ($180^\circ - \phi$) of Ru-O-Ru bonds, which becomes zero for BaRuO₃. Apart from slight distortions of RuO₆ octahedra in CaRuO₃ and SrRuO₃, that are absent in BaRuO₃⁸, each of these materials have threefold degenerate t_{2g} bands near the Fermi-level with a formal valance of 4 electrons⁸ i.e., $t_{2g}^4 e_g^0$. Density functional theory (DFT) calculations have been performed within the generalized gradient approximation using the plane wave pseudo-potential

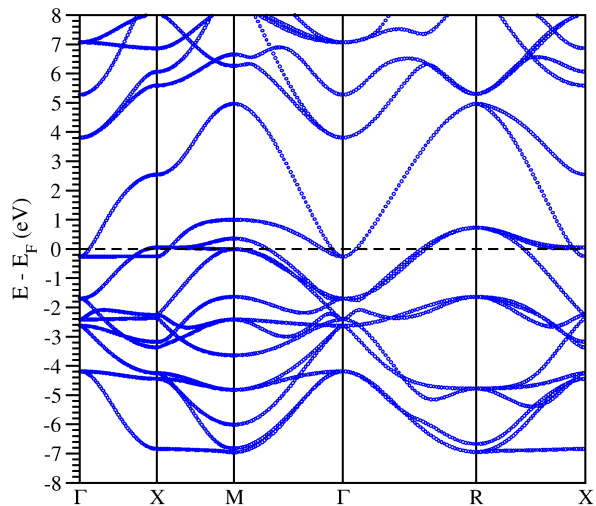


FIG. 1. (color online) Band-structure of cubic BaRuO₃ in its nonmagnetic phase. Energies are scaled to the Fermi-level (dotted line).

code QUANTUM ESPRESSO¹⁸. We have used ultra-soft pseudo-potentials with Perdew-Burke-Ernzerhof¹⁹ exchange-correlation functional. An $8 \times 8 \times 8$ Monkhorst-Pack k-grid is used for optimization together with an 80 Ry energy cutoff and a 640 Ry charge cutoff. The system is considered to be optimized if the forces acting on all the atoms are less than 10^{-4} Ry/Bohr. After optimization, we find the lattice parameter to be 4.0745 Å. Throughout the calculations, Marzari-Vanderbilt cold smearing is used with a degauss value of 0.01 Ry. A $20 \times 20 \times 20$ k-grid without any symmetries is used for all the nonself-consistent calculations (including Wannier90 calculations). To extract the information of the low-energy subspace, which will be used by the DMFT code, we have projected the Bloch wave-functions obtained from our DFT calculations on to the Ru- t_{2g} orbitals using the maximally localized Wannier functions²⁰ (MLWF) technique as implemented in the Wannier90 code²¹.

The electronic bandstructure, density of states (DOS) and projected DOS (pDOS) of BaRuO₃ in its non-magnetic (NM) phase are given in figures 1 and 2. The DFT results predict BaRuO₃ to be a metal in its non-magnetic phase with major contributions from the Ru-4d and O-2p orbitals across the Fermi-level. Hybridization between Ru-4d orbitals and O-2p orbitals spans from ~ -8 eV below the Fermi level to ~ 5 eV above the Fermi level. Bands above 5 eV are mainly composed of Ba-d orbitals and Ru-p orbitals.

We find that, due to the octahedral environment of

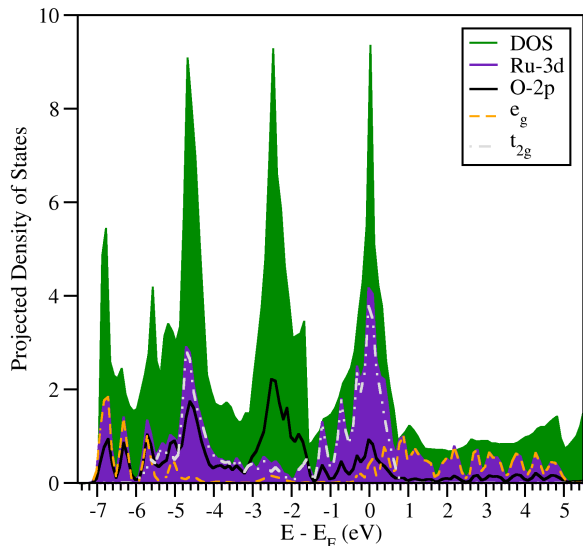


FIG. 2. (color online) Projected density of states (PDOS) of BaRuO₃. Green (shaded light gray), violet (shaded dark gray), black (thick line), gray (dotted and dashed line) and orange (dashed line) colors represents the DOS of whole system, Ru-atom, O-atom, Ru- t_{2g} and Ru- e_g , respectively.

the oxygen atoms surrounding the Ruthenium atoms, the Ru-4d orbitals split into two sets, namely, t_{2g} and e_g , where t_{2g} (e_g) orbitals contribution to the DOS is mainly below (above) Fermi-level, supporting the low-spin t_{2g} configuration of the nominal valence Ru⁴⁺ (d^4).

From figure 2, we infer that the low energy subspace (-2.5 to 1 eV) which is relevant for the DMFT calculations is mainly composed of the Ru- t_{2g} orbitals (with minor contributions of O-2p orbitals and Ru- e_g orbitals) have occupancy of ~ 4 electrons. Hence, to extract this low energy subspace Hamiltonian in an effective Wannier function basis, we have projected the Bloch-wave-functions obtained from our DFT calculations onto the d_{xz} , d_{yz} , and d_{xy} orbitals. The optimized Wannier functions calculated using the MLWF method as implemented in Wannier90²¹ code are given in figure 3 and the corresponding low energy subspace band-structure calculated using these Wannier functions are given in figure 4. Clearly, band-structures obtained from both the basis sets (Wannier, plane-wave) compare fairly well in the low energy subspace, validating the proper choice of our projections. Also, as shown in figure 3, the Wannier functions show the d_{xz} , d_{yz} , and d_{xy} orbital character and in addition have a substantial O-2p character due to their contributions near the Fermi-level. The $H(\mathbf{k})$ obtained in this Wannier basis is used for all the DMFT calculations, as the unperturbed or the ‘non-interacting’ Hamiltonian.

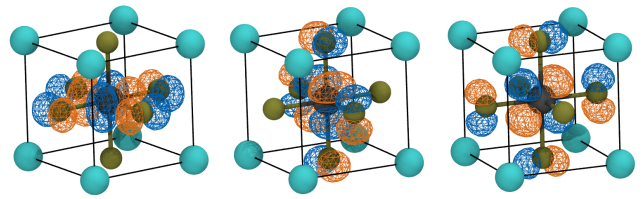


FIG. 3. (color online) Orbital plots of maximally localized Wannier functions used to reproduce the low energy subspace Hamiltonian.

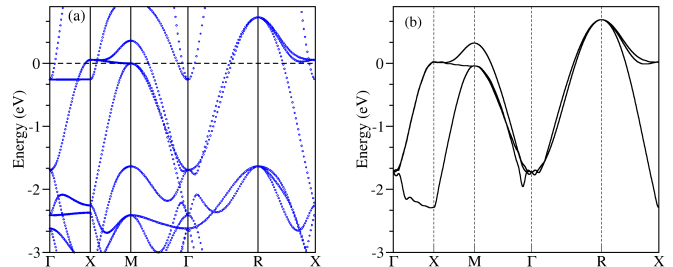


FIG. 4. (color online) Low energy subspace band-structure obtained from (a) Plane-wave basis and (b) Wannier basis.

III. GGA+DMFT:

In DMFT calculations we have introduced a local Coulomb interaction of density-density type between orbitals. The interaction part of the Hamiltonian is given in the second quantization notation by,

$$H_{ii}^{int} = \sum_{i\alpha=1}^3 U n_{i\alpha\uparrow} n_{i\alpha\downarrow} + \sum_{i\alpha \neq \beta} \sum_{\sigma\sigma'} (V - J\delta_{\sigma\sigma'}) n_{i\alpha\sigma} n_{i\beta\sigma'},$$

where i represents the lattice site and α, β represent orbital indices. U is the Coulomb repulsion between two electrons with opposite spin on the same orbital. We impose orbital rotational symmetry on the above Hamiltonian by setting $V = U - 2J$, where J is the Hund’s coupling, which lowers the energy of a configuration with different orbitals ($\alpha \neq \beta$), and parallel spins $\sigma = \sigma'$. We have solved the effective impurity problem within DMFT by using HY-CTQMC. In the literature, a range of U and J values have been used for 4d-Ru based TMOs. Indeed, determining these without ambiguity is not possible at present. In a recent work⁷, using the constrained random phase approximation (cRPA) method, the U value for ruthenates was found to be 2.3 eV. Thus, we choose $U_{Ru}=2.3$ eV. We fix the J_{Ru} such that the theoretically calculated paramagnetic magnetic moment matches the corresponding experimentally measured value. Apart from this specific set of model parameters, we have investigated a range of (U, J) values in the neighbourhood

of (U_{Ru}, J_{Ru}) to ascertain the position of 3C-BaRuO₃ in the phase diagram. In the DMFT calculations, we find the chemical potential by fixing the occupancy should be equal to 4 electrons per Ru, which is obtained from threefold degenerate t_{2g} bands in the Wannier basis or ‘non-interacting’ Hamiltonian. Now, we are going to discuss our results for single and two particle dynamics obtained from GGA+DMFT by using HY-CTQMC as an impurity solver.

A. Single Particle Dynamics:

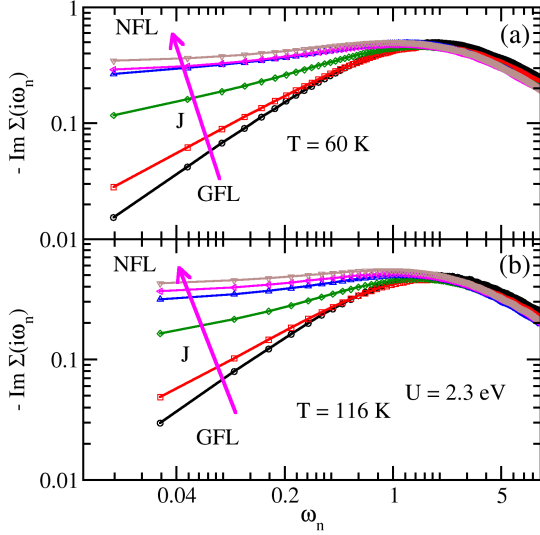


FIG. 5. (color online) Imaginary part of Matsubara self-energy ($-\text{Im}\Sigma(i\omega_n)$) for $U = 2.3$ eV and different J values for (a) $T = 60$ K (b) $T = 116$ K.

To begin with, we focus on single particle dynamics that is mainly determined by the self-energy $\Sigma(i\omega_n)$. Figure 5(a) shows the imaginary part of Matsubara self-energy for $U = 2.3$ eV and $T = 60$ K for a range of J values. For $J \lesssim 0.1$, the low-frequency behavior of self-energy has a generalized Fermi liquid (GFL) form i.e., $-\text{Im}\Sigma(i\omega_n) \sim a\omega_n^\alpha$ where $0 < \alpha \leq 1$. As we increase J , a deviation from the power law is seen at low ω_n as the $-\text{Im}\Sigma(i\omega_n)$ acquires a non-zero intercept. The latter is characteristic of non-Fermi liquid behaviour, where the imaginary part of self-energy has a finite value as $\omega_n \rightarrow 0$. Thus as a function of increasing J , the single particle dynamics exhibits a crossover from GFL to NFL that is driven by Hund’s exchange³. The crossover is found to persist at a higher temperature $T = 116$ K and is shown in figure 5(b).

A natural question arises about the choice of the

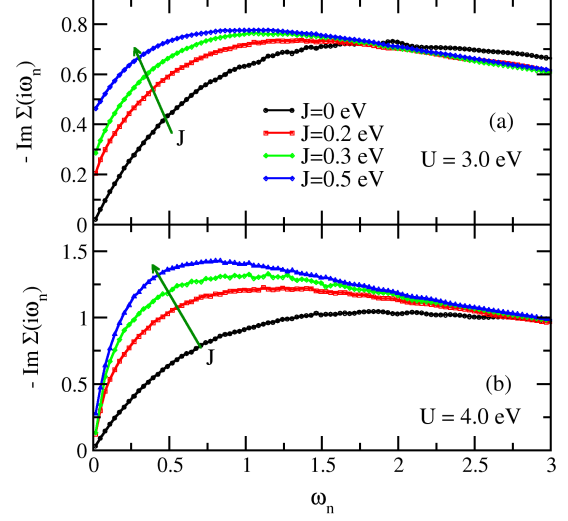


FIG. 6. (color online) Imaginary part of Self energy for $T = 60$ K and different J values (mentioned in legends) with (a) $U = 3$ eV, and (b) $U = 4$ eV.

$U = 2.3$ eV for 3C-BaRuO₃. Does this crossover from GFL to NFL survive with respect to variations in U ? The imaginary part of self-energy for $U = 3$ and 4 eV computed at a temperature, $T = 60$ K is shown in figure 6. Clearly, for $U = 2.3$ and 3 eV, the intercept of the imaginary part of the self-energy is finite for $J \gtrsim 0.2$ (from figure 5 and the top panel of figure 6), while for $U = 4$ eV, a GFL form of $-\text{Im}\Sigma(i\omega_n)$ is obtained for $0 \leq J \leq 0.5$ eV. This implies that the NFL behaviour for higher values of $U (\gtrsim 4)$ eV, if at all occurs, must be for $J > 0.5$ eV. Hence, we conclude that the $U_{Ru} = 2.3$ eV, corresponding to 3C-BaRuO₃ is somewhat special, since it places this material in a crossover region for *physically reasonable* values of the Hund’s exchange.

It is known from recent works on ruthenates that the NFL behaviour seen in the single-particle dynamics is characteristic of a finite temperature spin-frozen phase which crosses over to a Fermi liquid ground state at lower temperatures. This incoherent spin-frozen state⁶ is characterised by finite intercepts in the imaginary part of self-energy and fluctuating local moments (through susceptibility). In order to understand the crossover phase in a better way, we carry out a quantitative analysis of the imaginary part of the self-energy for many more J values in the same range as considered in figure 5. The imaginary part of self-energy at low Matsubara frequencies is fit to the form³

$$-\text{Im}\Sigma(i\omega_n) \xrightarrow{\omega_n \rightarrow 0} C + A|\omega_n|^\alpha, \quad (1)$$

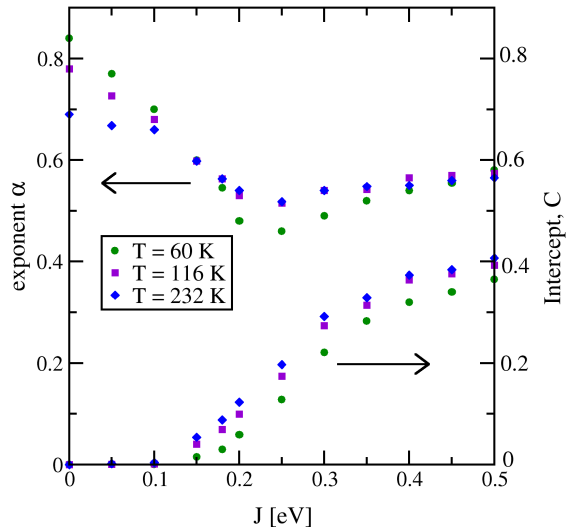


FIG. 7. (color online) Exponent α (left) and intercept C (right) obtained by fitting the data to $-\text{Im } \Sigma(i\omega_n) = C + A|\omega_n|^\alpha$ at different J values, $U = 2.3$ eV and $T = 60$ K, 116K and 232K.

and figure 7 shows the exponent α (circles) and intercept C (squares) as a function of J at various temperatures from 60K to 230K, for $U = 2.30$ eV. The exponent α initially decreases with increasing J , goes through a minimum value of 0.5 at a $J \sim 0.25$ eV and increases gradually for higher J . Such behaviour has been found previously by Werner³ et. al., in a three orbital Hubbard model with fully rotationally invariant interactions for fixed filling ($n=2.0$) and Hund's exchange, but varying the U value. The intercept C remains zero for $J \lesssim 0.15$ eV and above that it has a finite value which increases with J . Thus we identify a crossover Hund's exchange $J_0 = 0.15$ eV such that for $J < J_0$ the GFL phase exists, while for $J > J_0$ the crossover NFL phase is found for $\gtrsim 60$ K, where frozen moments are expected to scatter the conduction electrons. It is interesting to note that the exponent α in the GFL or in the NFL region is not equal to 1. In the GFL phase, the exponent must approach 1 with decreasing temperature, and indeed, it does, as seen in figure 7 for $J < J_0$. Curiously, the exponent hardly changes with either temperature or J in the spin-frozen phase even until 60K. For 3C-BaRuO₃, a ferromagnetic transition occurs at $T_c = 60$ K. Thus, it is likely that the spin-frozen phase is a precursor of the FM phase, and the local moments condense into a magnetically ordered state for $T < 60$ K. We have repeated the above analysis for $U = 3$ eV and find that the crossover $J_0 \sim 0.15$ eV is the same as that for $U = 2.3$ eV within numerical tolerance. Even the intercept depends very weakly on temperature, thus, the spin-frozen phase appears to be

almost temperature independent. This implies that the NFL behaviour should manifest in transport and thermodynamic quantities over a wide range from about 60K to at least 230K.

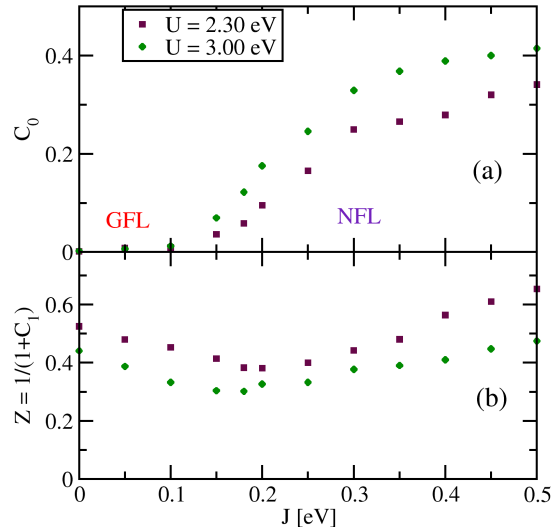


FIG. 8. (color online) Imaginary part of self energy ($-\text{Im } \Sigma(i\omega_n)$) fitted to 4th order polynomial: (a) zeroth order coefficient, C_0 (b) $Z = 1/(1+C_1)$, where C_1 is the linear coefficient, for different J values, $U=2.3$ and 3.0 eV and $T = 60$ K.

The crossover function, given in equation 1 does not have a microscopic basis, and has been used purely as a fitting function. Since the latter is not unique, the identification of J_0 must be verified through an alternative fit. Hence, we have used a fourth order polynomial also to fit $-\text{Im}\Sigma(i\omega_n)$ and confirm the robustness of J_0 . The intercept C_0 shown in the top panel of figure 8 does become non-zero only for $J \gtrsim J_0$. Thus, the identification of J_0 remains robust. For a Fermi liquid, the linear coefficient of the self-energy, C_1 is related to the quasiparticle weight, Z by $C_1 = -(1 - 1/Z)$ at $T = 0$. Although C_1 does not have the same interpretation at finite temperature, a qualitative picture may be obtained by examining the dependence of $Z = 1/(1 + C_1)$. The lower panel of figure 8 shows that the Z decreases throughout the GFL phase. Although the Z lacks any interpretation in the NFL phase ($J > J_0$), a finite Z is, nevertheless, obtained which behaves in a similar way as the exponent of the power law fit (figure 7).

B. Two Particle Dynamics:

The effect of temperature on spin correlations may be gauged through the local static spin susceptibility, given

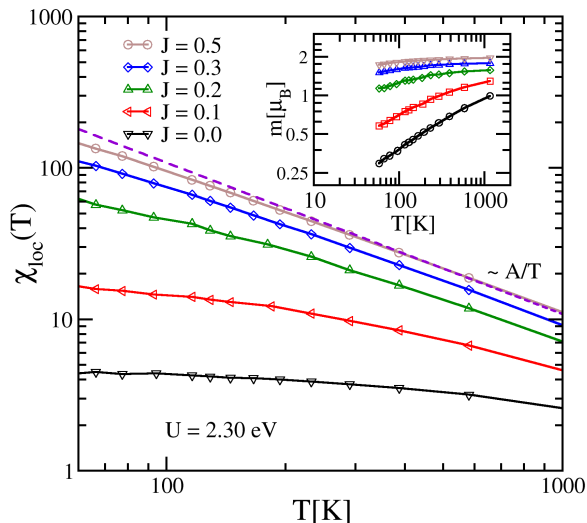


FIG. 9. (online) Local static spin susceptibility as a function of temperature for different J values and $U = 2.30$ eV. The dashed curve represents a $1/T$ fit at high temperatures. Inset: The screened magnetic moment as a function of temperature.

by $\chi_{loc}(T) = \int_0^\beta d\tau \chi_{zz}(\tau)$. Figure 9, shows $\chi_{loc}(T)$ as a function of temperature for a range of J values. For $J \lesssim 0.1$, $\chi_{loc}(T)$ is very weakly dependent of temperature over the entire range shown, which is characteristic of Pauli-paramagnetic behavior and hence corresponds to a GFL behaviour. For larger J values, we observe local moment behavior ($\chi_{loc}(T) \sim \frac{1}{T}$) behaviour at lower temperatures as well (see dashed line fit in the main panel). Thus with increasing J , χ_{loc} also crosses over to local moment region from GFL regime. We will see later that the temperature dependence of susceptibility allows to identify the value of Hund's exchange coupling appropriate for 3C-BaRuO₃. The inset shows the screened magnetic moment as a function of temperature computed through^{22,23} $m = \sqrt{T\chi(T)}$. In the GFL phase ($J < J_0$), the magnetic moment is seen to decrease monotonically with decreasing temperature indicating an absence of local moments at $T = 0$. While for $J > J_0$, the magnetic moment *appears* to saturate as $T \rightarrow 0$ indicating fluctuating incoherent local-moments in the spin-frozen phase.

In most of the 4d Ru-based TM oxides, most theoretical studies are restricted to single-particle spectral functions and static susceptibilities^{4,6}. There are only a few studies on two particle spectral functions including vertex corrections²⁴, and even those are limited to fixed U and J values. However, there are no studies available for the behavior of two particle spectral functions (including vertex corrections) across the GFL to NFL crossover.

We have calculated the dynamical spin susceptibility $\chi(\omega, T)$ on the real frequency axis by using maximum

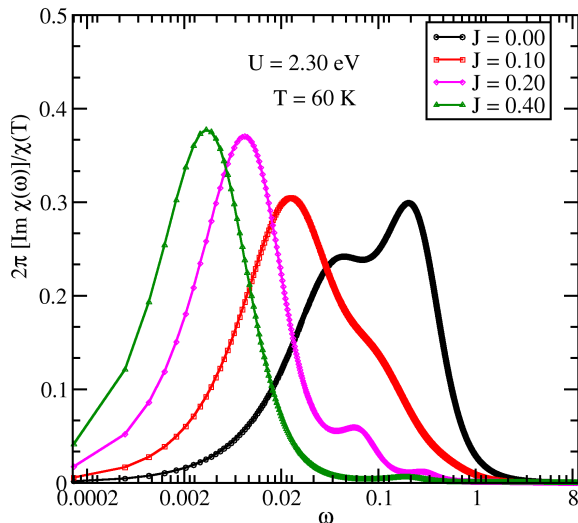


FIG. 10. (color online) Imaginary part of dynamical spin susceptibility on real frequency axis obtained from maximum entropy method for various J values, $U = 2.3$ eV and $T = 60$ K.

entropy method²⁵⁻²⁷. In figure 10, we show the imaginary part of $\chi(\omega, T)$ for various J values at $U = 2.30$ eV and $T = 60$ K. A large scale spectral weight transfer to the infrared occurs upon increasing J of $\chi(\omega, T)$. Concomitantly, the half-width at half maximum also decreases. The peak in $\chi(\omega, T)$ represents the characteristic energy scale of the system^{24,28}, below which a Fermi liquid should emerge. The dramatic red shift of the peak with increasing J implies a strong suppression of the coherent scale²⁸⁻³⁰. Thus with increasing J , the energy scale for crossover from a low temperature Fermi liquid ground state to a high temperature incoherent phase decreases sharply. Since the only other scale (apart from the coherence scale) are the non-universal scales such as J or the bandwidth or U , the incoherent crossover phase should exist from very low temperatures to quite high temperatures. This explains the wide temperature range over which an incoherent spin-frozen phase, and the corresponding non-Fermi liquid behaviour is found, e.g in the resistivity^{1,8,11}.

C. Identification of J for 3C-BaRuO₃

Now we turn to an identification of model parameters appropriate for 3C-BaRuO₃ in the (U, J) plane. As mentioned earlier, we have chosen $U_{Ru} = 2.3$ eV for 3C-BaRuO₃ which has been obtained through cRPA for its closely related cousins in the ruthenate family^{6,7,31}. The J_{Ru} is obtained by comparing the theoretically

computed, temperature dependent, static susceptibility (from figure 9) with that of the experiment⁸. From experiments, it is known that the saturated magnetic moment at 5K (in the ferromagnetic state) is $0.8\mu_B/\text{Ru}$, while the high temperature paramagnetic moment is $2.6\mu_B/\text{Ru}$. Since our theory is valid only in the non-magnetic phase, we choose the latter for theoretical comparison. One more issue in the theory is the use of Ising-type or density-density type Hund's coupling, which results in a $S = 1$ state corresponding to an ideal magnetic moment of $2\mu_B/\text{Ru}$ rather than $2.8\mu_B$ as would be expected for a true $S = 1$ state with a rotationally invariant J term. Thus, the high temperature moment that we would be comparing to is $(2.6/2.8) \times 2 = 1.86\mu_B/\text{Ru}$. We see from the inset of figure 9 that such a moment is obtained for $J \sim 0.5$ eV. Hence we identify $J_{Ru} \sim 0.5$ eV. We note that the experimentally measured $\chi_{loc}^{-1}(T)$ is linear at high temperature, and deviates from linearity⁸ at $T \lesssim 150\text{K}$. Again, such deviation from the high temperature $1/T$ form in theoretical calculations is seen for $J \sim 0.5$ at $T \lesssim 150\text{K}$ (in the main panel of figure 9), thus lending support to the identification of $J_{Ru} \sim 0.5$ eV from the magnetic moment. We have checked that the deviations from linearity occur at much higher temperatures ($\gtrsim 300\text{K}$) for $J = 0.3$ and 0.4eV , hence the error bar on J_{Ru} should be less than 0.1eV .

The value of Hund's coupling $J_{Ru} \sim 0.5$ eV places 3C-BaRuO_3 deep in the incoherent spin-frozen phase for $T \gtrsim 60\text{K}$, and thus could explain the transition into a magnetically ordered state at $T \lesssim 60\text{K}$. The experimentally observed non-Fermi liquid behavior in $\rho(T)$ could originate from an anomalous self-energy. Indeed as figure 9 shows, the self-energy at the chemical potential has a finite and almost temperature-independent imaginary part. In addition to the static part, it would be interesting to see if the dynamics also contributes to the NFL behaviour. Hence, we compute the real frequency self-energy through analytic continuation of the Matsubara $\Sigma(i\omega_n)$ and display $-\text{Im}\Sigma(\omega)$ (top panel) and the corresponding k -integrated spectrum, $A(\omega) = -\text{Im}G(\omega)$ (bottom panel) for various temperatures in figure 11, where the local Green's function is given by

$$\begin{aligned} \mathbf{G}(\omega) &= \sum_k \mathbf{G}(k, \omega) \\ &= \sum_k \frac{1}{(\omega^+ + \mu)\mathbf{I} - \mathcal{H}_{\mathbf{GGA}}(k) - \Sigma(\omega)}. \end{aligned} \quad (2)$$

Note that, within DMFT, the k -dependence arises purely through the dispersion embedded in $\mathcal{H}_{\mathbf{GGA}}(k)$. If the low energy excitations are Fermi-liquid like, then we should expect $\text{Im} \Sigma(0) \propto -T^2$. However the almost temperature-independent and finite value of $\text{Im} \Sigma(0)$ shown previously in figure 7 and also seen in figure 11(a) signifies that low energy excitations are NFL in nature, and temperature does not have much effect on the value of $\text{Im} \Sigma(0)$ in the spin-frozen phase. A very interesting insight into the dynamics of the spin-frozen phase comes

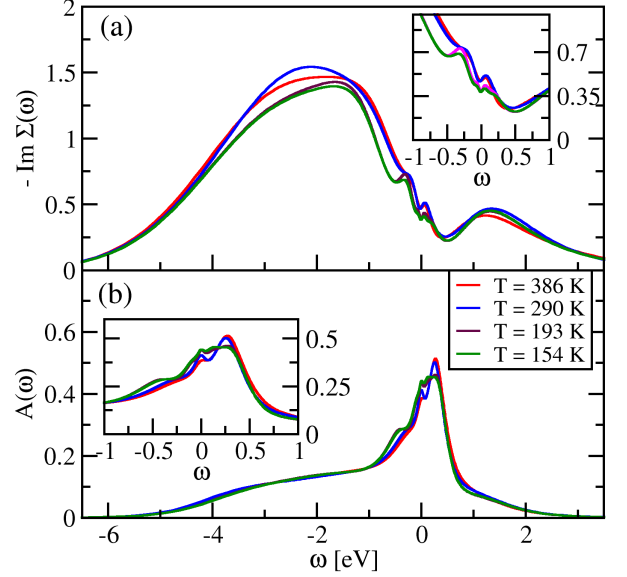


FIG. 11. (color online) (a) Imaginary part of self-energy (b) single particle spectral function on real frequency axis obtained from maximum entropy method for different temperatures and $U = 2.3$ eV, $J = 0.5$ eV.

from the low frequency form of the self-energy. The inset zooms in onto the low frequency part of $-\text{Im}\Sigma(\omega)$, which is seen to have a form $\sim C + A\omega^2$ that is usually found in disordered Fermi liquids³². Such a form is consistent with the scenario of incoherent and fluctuating local moments in the spin-frozen phase. The single-particle spectral function $A(\omega)$ shown in figure 11(b) has an overall line-shape very similar to that of SrRuO_3 ³³ and Sr_2RuO_4 ¹. A metallic nature is indicated by a finite weight at the Fermi level. A closer look at the temperature dependence at low frequencies shows the emergence of structures that presumably correspond to transitions between the various multiplets of the atomic limit. However, a far more detailed study, varying U and J , is required for a precise identification of the origin of these features. Since the procedure of analytic continuation using the maximum entropy method requires immense computational resources, especially in the spin-frozen phase, we have not attempted to carry out such a study in the present work.

Experiments can probe single-particle dynamics in the spin-frozen phase through e.g. angle-resolved photoemission spectroscopy (ARPES). Theoretically we can predict the ARPES lineshape through a calculation of the k -resolved spectral function is given by $A(k, \omega) = -\text{Im}G(k, \omega)/\pi$. In figure 12 we have plotted the intensity map of the momentum-resolved spectral function $A(k, \omega)$

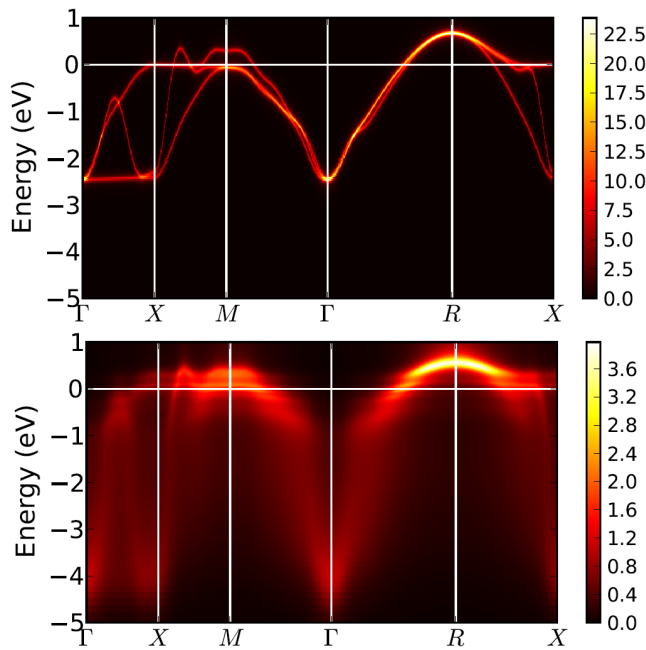


FIG. 12. (color online) Intensity map of the spectral function $A(k, \omega)$ obtained from DFT (top panel) and DFT+DMFT (lower panel) for $U = 2.3$ eV, $J = 0.5$ eV at $T=154$ K plotted along high symmetry directions in the irreducible Brillouin zone.

of 3C-BaRuO₃ obtained from DFT (top panel, obtained by simply ignoring the self-energy in equation 2) and then compared with the results of DFT+DMFT (lower panel) at $T = 154$ K for $U_{Ru} = 2.3$ eV and $J_{Ru} = 0.5$ eV. In case of DFT, the quasi-particle bands have a minimum at Γ point (-2.3 eV) and maximum at R point (0.8 eV). When we turn on interactions (in the case of DFT+DMFT), the first striking feature that emerges is that there are no quasiparticle bands. In other words, each of the bands obtained within DFT acquires a finite width when interactions are introduced, but there does exist a resemblance of the quasiparticle bands in the spectral function map. The ‘fat bands’ are simply a result of the finite scattering rate arising from the imaginary part of the self-energy (figure 11). Furthermore, although the bands in DFT as well as DFT+DMFT have a minimum and maximum exactly at the same high symmetry points, the values of corresponding energies renormalize to -4.8 and 1.0 eV respectively in the latter. The bands below -1.0 eV (incoherent regime) are much more broadened^{6,33} in comparison with the those closer to the Fermi-level, which again is a manifestation of the peak in the imaginary part of the self-energy around -2 eV.

For the values of $U_{Ru}=2.3$ eV and $J_{Ru} \sim 0.5$ eV, we obtain a relatively modest effective mass $\frac{m^*}{m_{GGA}}$ of 1.56 at $T = 60$ K. A definitive comment about the effective mass in the ground state cannot be made with the preceding estimate at finite temperature, since the quasiparticle weight has a proper meaning³⁴ only below the Fermi liquid coherence scale, which is strongly suppressed for

$J = 0.5$ (as compared to $J = 0$) as seen from the dynamical susceptibility results (from figure 10). Thus, unless extremely low temperature calculations are carried out, a proper estimate of m^* is not possible. Nevertheless, the strong suppression of the Fermi liquid scale suggests that 3C-BaRuO₃ could be very strongly correlated. Here, we would like to comment on the value of U (= 4.0 eV) and J (= 0.6 eV) chosen in a previous work³⁵ on 3C-BaRuO₃ within the dpp model. They obtained the interaction parameters from a “local spin density approximation constraint” technique. For those parameters, a recent study of one of the 4d Ruthenium compounds⁷ within a five d-band model finds that correlations are induced due to the proximity of a Mott insulating state, which concurs with our results for a three d-band model (from the lower panel of figure 2). However, the proximity of a Mott insulating state does not violate adiabatic continuity and hence as shown above, the choice of $(U, J) = (4.0, 0.6)$ eV would not explain several anomalous features of 3C-BaRuO₃ including the wide $1/T$ behaviour of $\chi_{loc}(T)$, or the NFL behaviour of resistivity. These and the transition to a ferromagnetically ordered state at low temperature are naturally explained by the presence of a spin-frozen phase as found for $U_{Ru} = 2.3$ eV and $J_{Ru} \sim 0.5$ eV.

IV. Conclusions

We have studied the 3C-BaRuO₃ in the non-magnetic phase by using GGA+DMFT (HY-CTQMC). In the dynamical correlation functions and static spin susceptibility, we observed a crossover from GFL to NFL driven by the Hund’s exchange J and a fitting of the self-energy to a power law function (ω_n^α) determined the cross-over boundary i.e., $J_0 = 0.15$ eV. The local, on-site Coulomb repulsion, $U_{Ru} = 2.3$ eV, was chosen to be the same as that found through constrained random phase approximation calculations for the closely related SrRuO₃. We determine the Hund’s exchange, J_{Ru} , appropriate for 3C-BaRuO₃ such that the computed high temperature paramagnetic moment matches the experimentally found value, and thus we find that $J_{Ru} \sim 0.5$ eV. Non-magnetic calculations with these parameters (U_{Ru} , J_{Ru}) for single-particle dynamics and static spin susceptibility show that cubic-BaRuO₃ is in a spin-frozen state at temperatures above the ferromagnetic transition point. Future calculations incorporating symmetry broken states should reveal the causal relation between the high temperature spin-frozen phase and the dynamics in the low temperature ferromagnetic phase.

V. Acknowledgments

We thank CSIR and DST (India) for research funding. This work is partly supported by NSF DMR-1237565 (NSV and JM) and NSF EPSCoR Cooperative Agree-

ment EPS-1003897 with additional support from the Louisiana Board of Regents (ND and MJ). ND thank Swapan K. Pati for helpful discussions. Our simulations used an open source implementation³⁶ of the hybridization expansion continuous-time quantum Monte Carlo

algorithm¹⁷ and the ALPS³⁷ libraries. The computational resources for CTQMC simulations are provided by the Louisiana Optical Network Initiative (LONI) and HPC@LSU.

-
- * nagamalleswararao.d@gmail.com
† raja@jncasr.ac.in
- ¹ A. Georges, L. d. Medici, and J. Mravlje, *Annu. Rev. Condens. Matter Phys.* **4**, 137 (April 2013), <http://www.annualreviews.org/doi/pdf/10.1146/annurev-conmatphys-020911-125045>
 - ² J. Zhao, L. Yang, Y. Yu, F. Li, R. Yu, Z. Fang, L. Chen, and C. Jin, *Journal of Solid State Chemistry* **180**, 2816 (2007), ISSN 0022-4596, <http://www.sciencedirect.com/science/article/pii/S0022459607003027>
 - ³ P. Werner, E. Gull, M. Troyer, and A. J. Millis, *Phys. Rev. Lett.* **101**, 166405 (Oct 2008), <http://link.aps.org/doi/10.1103/PhysRevLett.101.166405>
 - ⁴ K. Haule and G. Kotliar, *New Journal of Physics* **11**, 025021 (2009), <http://stacks.iop.org/1367-2630/11/i=2/a=025021>
 - ⁵ L. de' Medici, J. Mravlje, and A. Georges, *Phys. Rev. Lett.* **107**, 256401 (Dec 2011), <http://link.aps.org/doi/10.1103/PhysRevLett.107.256401>
 - ⁶ J. Mravlje, M. Aichhorn, T. Miyake, K. Haule, G. Kotliar, and A. Georges, *Phys. Rev. Lett.* **106**, 096401 (Mar 2011), <http://link.aps.org/doi/10.1103/PhysRevLett.106.096401>
 - ⁷ H. T. Dang, J. Mravlje, A. Georges, and A. J. Millis, *Phys. Rev. B* **91**, 195149 (May 2015), <http://link.aps.org/doi/10.1103/PhysRevB.91.195149>
 - ⁸ C.-Q. Jin, J.-S. Zhou, J. B. Goodenough, Q. Q. Liu, J. G. Zhao, L. X. Yang, Y. Yu, R. C. Yu, T. Katsura, A. Shatskiy, and E. Ito, *Proceedings of the National Academy of Sciences* **105**, 7115 (2008), <http://www.pnas.org/content/105/20/7115.abstract>
 - ⁹ G. Cao, S. McCall, M. Shepard, J. E. Crow, and R. P. Guertin, *Phys. Rev. B* **56**, 321 (Jul 1997), <http://link.aps.org/doi/10.1103/PhysRevB.56.321>
 - ¹⁰ J.-S. Zhou, K. Matsubayashi, Y. Uwatoko, C.-Q. Jin, J.-G. Cheng, J. B. Goodenough, Q. Q. Liu, T. Katsura, A. Shatskiy, and E. Ito, *Phys. Rev. Lett.* **101**, 077206 (Aug 2008), <http://link.aps.org/doi/10.1103/PhysRevLett.101.077206>
 - ¹¹ P. B. Allen, H. Berger, O. Chauvet, L. Forro, T. Jarlborg, A. Junod, B. Revaz, and G. Santi, *Phys. Rev. B* **53**, 4393 (Feb 1996), <http://link.aps.org/doi/10.1103/PhysRevB.53.4393>
 - ¹² Y. S. Lee, J. Yu, J. S. Lee, T. W. Noh, T.-H. Gimm, H.-Y. Choi, and C. B. Eom, *Phys. Rev. B* **66**, 041104 (Jul 2002), <http://link.aps.org/doi/10.1103/PhysRevB.66.041104>
 - ¹³ G. Kotliar, S. Y. Savrasov, K. Haule, V. S. Oudovenko, O. Parcollet, and C. A. Marianetti, *Rev. Mod. Phys.* **78**, 865 (Aug 2006), <http://link.aps.org/doi/10.1103/RevModPhys.78.865>
 - ¹⁴ J. P. Perdew, K. Burke, and M. Ernzerhof, *Phys. Rev. Lett.* **77**, 3865 (Oct 1996), <http://link.aps.org/doi/10.1103/PhysRevLett.77.3865>
 - ¹⁵ A. Georges, G. Kotliar, W. Krauth, and M. J. Rozenberg, *Rev. Mod. Phys.* **68**, 13 (Jan 1996), <http://link.aps.org/doi/10.1103/RevModPhys.68.13>
 - ¹⁶ E. Gull, A. J. Millis, A. I. Lichtenstein, A. N. Rubtsov, M. Troyer, and P. Werner, *Rev. Mod. Phys.* **83**, 349 (May 2011), <http://link.aps.org/doi/10.1103/RevModPhys.83.349>
 - ¹⁷ P. Werner, A. Comanac, L. de' Medici, M. Troyer, and A. J. Millis, *Phys. Rev. Lett.* **97**, 076405 (Aug 2006), <http://link.aps.org/doi/10.1103/PhysRevLett.97.076405>
 - ¹⁸ P. Giannozzi, S. Baroni, N. Bonini, M. Calandra, R. Car, C. Cavazzoni, D. Ceresoli, G. L. Chiarotti, M. Cococcioni, I. Dabo, A. Dal Corso, S. de Gironcoli, S. Fabris, G. Fratesi, R. Gebauer, U. Gerstmann, C. Gougousis, A. Kokalj, M. Lazzeri, L. Martin-Samos, N. Marzari, F. Mauri, R. Mazzarello, S. Paolini, A. Pasquarello, L. Paulatto, C. Sbraccia, S. Scandolo, G. Sciauzero, A. P. Seitsonen, A. Smogunov, P. Umari, and R. M. Wentzcovitch, *Journal of Physics: Condensed Matter* **21**, 395502 (19pp) (2009), <http://www.quantum-espresso.org>
 - ¹⁹ J. P. Perdew, K. Burke, and Y. Wang, *Phys. Rev. B* **54**, 16533 (Dec 1996), <http://link.aps.org/doi/10.1103/PhysRevB.54.16533>
 - ²⁰ N. Marzari and D. Vanderbilt, *Phys. Rev. B* **56**, 12847 (Nov 1997), <http://link.aps.org/doi/10.1103/PhysRevB.56.12847>
 - ²¹ A. A. Mostofi, J. R. Yates, Y.-S. Lee, I. Souza, D. Vanderbilt, and N. Marzari, *Computer Physics Communications* **178**, 685 (2008), ISSN 0010-4655, <http://www.sciencedirect.com/science/article/pii/S0010465507004936>
 - ²² H. R. Krishna-murthy, J. W. Wilkins, and K. G. Wilson, *Phys. Rev. B* **21**, 1003 (Feb 1980), <http://link.aps.org/doi/10.1103/PhysRevB.21.1003>
 - ²³ P. Hansmann, R. Arita, A. Toschi, S. Sakai, G. Sangiovanni, and K. Held, *Phys. Rev. Lett.* **104**, 197002 (May 2010), <http://link.aps.org/doi/10.1103/PhysRevLett.104.197002>
 - ²⁴ A. Toschi, R. Arita, P. Hansmann, G. Sangiovanni, and K. Held, *Phys. Rev. B* **86**, 064411 (Aug 2012), <http://link.aps.org/doi/10.1103/PhysRevB.86.064411>
 - ²⁵ M. Jarrell and J. E. Gubernatis, *Physics Reports* **269**, 133 (Jan 1996)
 - ²⁶ M. Jarrell, J. E. Gubernatis, and R. N. Silver, *Phys. Rev. B* **44**, 5347 (Sep 1991), <http://link.aps.org/doi/10.1103/PhysRevB.44.5347>
 - ²⁷ N. Dasari, J. Moreno, N. S. Vidhyadhiraja, and M. Jarrell, "Analytic continuation of hybridization expansion continuous-time quantum Monte-Carlo data using the maximum entropy method," unpublished
 - ²⁸ M. Jarrell, J. E. Gubernatis, and R. N. Silver, *Phys. Rev. B* **44**, 5347 (Sep 1991), <http://link.aps.org/doi/10.1103/PhysRevB.44.5347>

- ²⁹ C. Raas and G. S. Uhrig, Phys. Rev. B **79**, 115136 (Mar 2009), <http://link.aps.org/doi/10.1103/PhysRevB.79.115136>
- ³⁰ N. Dasari, S. Acharya, A. Taraphder, J. Moreno, M. Jarrell, and N. Vidhyadhiraja, arXiv preprint arXiv:1509.09163(2015)
- ³¹ Z. V. Pchelkina, I. A. Nekrasov, T. Pruschke, A. Sekiyama, S. Suga, V. I. Anisimov, and D. Vollhardt, Phys. Rev. B **75**, 035122 (Jan 2007), <http://link.aps.org/doi/10.1103/PhysRevB.75.035122>
- ³² N. S. Vidhyadhiraja and P. Kumar, Phys. Rev. B **88**, 195120 (Nov 2013), <http://link.aps.org/doi/10.1103/PhysRevB.88.195120>
- ³³ M. Kim and B. I. Min, Phys. Rev. B **91**, 205116 (May 2015), <http://link.aps.org/doi/10.1103/PhysRevB.91.205116>
- ³⁴ L. Fanfarillo and E. Bascones, Phys. Rev. B **92**, 075136 (Aug 2015), <http://link.aps.org/doi/10.1103/PhysRevB.92.075136>
- ³⁵ L. Huang and B. Ao, Phys. Rev. B **87**, 165139 (Apr 2013), <http://link.aps.org/doi/10.1103/PhysRevB.87.165139>
- ³⁶ H. H. Hafermann, P. Werner, and E. Gull, Computer Physics Communications, 184, 1280 (2013)
- ³⁷ B. Bauer, L. D. Carr, H. G. Evertz, A. Feiguin, J. Freire, S. Fuchs, L. Gamper, J. Gukelberger, E. Gull, S. Guertler, A. Hehn, R. Igarashi, S. V. Isakov, D. Koop, P. N. Ma, P. Mates, H. Matsuo, O. Parcollet, G. Pawowski, J. D. Picon, L. Pollet, E. Santos, V. W. Scarola, U. Schollwck, C. Silva, B. Surer, S. Todo, S. Trebst, M. Troyer, M. L. Wall, P. Werner, and S. Wessel, Journal of Statistical Mechanics: Theory and Experiment **2011**, P05001 (2011), <http://stacks.iop.org/1742-5468/2011/i=05/a=P05001>